The Astrophysical Journal Letters, 896:L5 (8pp), 2020 June 10 https://doi.org/10.3847/2041-8213/ab9531
© 2020. The Author(s). Published by the American Astronomical Society.
OPEN ACCESS

Quiet-time Solar Wind Suprathermal Electrons of Different Solar Origins

Liu Yang[1], Linghua Wang[1], Liang Zhao[2], Jiawei Tao[1], Gang Li[3], Robert F. Wimmer–Schweingruber[4,5], Jiansen He[1], Hui Tian[1], and Stuart D. Bale[6,7]
[1] School of Earth and Space Sciences, Peking University, Beijing, 100871, People's Republic of China; wanglhwang@gmail.com, wanglhwang@pku.edu.cn
[2] Department of Atmospheric, Oceanic, and Space Sciences, University of Michigan, Ann Arbor, MI 48105, USA
[3] Department of Space Science and CSPAR, University of Alabama in Huntsville, Huntsville, AL 35899, USA
[4] Institute of Experimental and Applied Physics, University of Kiel, Leibnizstrasse 11, D-24118 Kiel, Germany
[5] National Space Science Center, Beijing, 100190, People's Republic of China
[6] Physics Department, University of California, Berkeley, CA 94720-7300, USA
[7] Space Sciences Laboratory, University of California, Berkeley, CA 94720-7450, USA
Received 2020 April 30; revised 2020 May 20; accepted 2020 May 20; published 2020 June 8

Abstract

The energy spectrum of solar wind strahl, halo, and superhalo electrons likely carries crucial information on their possible origin and acceleration at the Sun. Here we statistically investigate the energy spectrum of solar wind strahl/halo electrons at ~0.1–1.5 keV and superhalo electrons at ~20–200 keV measured by Wind/3D Plasma and Energetic Particle during quiet times from 1998 to 2014, according to the types of their Potential Field Source Surface–mapped coronal source regions (CSRs). We adopt the classification scheme developed by Zhao et al. to categorize the CSRs into four types: active region (AR), quiet Sun (QS), coronal hole (CH), and helmet-streamer associated region (HS). We find that for the quiet-time strahl, the AR and HS (QS and CH) correspond to a smaller (larger) kappa index $\kappa_{\rm strahl}$ with the most frequent value of 7–8.5 (8.5–10) and a larger (smaller) $n_{\rm strahl}$ with the most frequent value of 0.013–0.026 $\rm cm^{-3}$ (0.006–0.0013 $\rm cm^{-3}$). For the quiet-time halo, $\kappa_{\rm halo}$ behaves similarly to $\kappa_{\rm strahl}$, but $n_{\rm halo}$ appears similar among the four CSR types. For the superhalo, the AR (QS) corresponds to a larger (smaller) power-law index β with the most frequent value of 2.2–2.4 (1.8–2.0), while the HS and CH have a β not different from either the AR or QS; $n_{\rm sup}$ appears similar, with the most frequent value of 3×10^{-8}–3×10^{-7} $\rm cm^{-3}$, among the four CSR types. These results suggest that the strahl (superhalo) from the hotter CSRs tends to be more (less) efficiently accelerated.

Unified Astronomy Thesaurus concepts: Solar physics (1476); Solar particle emission (1517); Solar wind (1534)

1. Introduction

The solar wind suprathermal electrons observed in the interplanetary medium (IPM) generally consist of three populations: a near-isotropic halo and a strongly field-aligned strahl, both with a kappa-function spectrum, at energies above thermal up to ~2 keV (e.g., Montgomery et al. 1968; Pilipp et al. 1987; Maksimovic et al. 2005; Tao et al. 2016; Wilson et al. 2019a, 2019b, 2020), as well as a nearly isotropic superhalo with a power-law spectrum at energies above ~2 keV (Lin 1998; Wang et al. 2012, 2015; Yang et al. 2015a). The formation mechanisms of these suprathermal electrons are still not fully understood. It is widely thought that the field-aligned strahl comes from escaping thermal electrons from the corona, while the halo could be formed due to the scattering of strahl in the IPM (e.g., Feldman et al. 1975; Pilipp et al. 1987; Štverák et al. 2009). Many theories/models have been proposed to explain the formation of the kappa-function spectrum: e.g., the kinetic exospheric model of the solar wind (Maksimovic et al. 1997; Pierrard et al. 2001) and a quasilinear theory of resonant interactions between the strahl/halo and whistler waves (Vocks et al. 2005; Yoon et al. 2006; Saito et al. 2008; Saito & Gary 2012; Chang et al. 2013; Hughes et al. 2014; Kim et al. 2015). For the superhalo's formation, Wang et al. (2012, 2015) proposed that superhalo electrons could originate from nonthermal processes related to the acceleration of solar wind (e.g., nanoflares; Parker 1988), followed by strong scattering/reflection in the IPM, or they could be due to the acceleration throughout the IPM by interplanetary shocks, waves, and/or stochastic processes (e.g., Fisk et al. 2010; Yoon et al. 2012; Zank et al. 2014; Yang et al. 2018, 2019).

The energy spectrum of solar wind suprathermal electrons would carry crucial information on their origin and formation. According to a statistical survey of strahl and halo energy spectra observed by the Wind 3D Plasma and Energetic Particle (3DP; Lin et al. 1995) instrument, Tao et al. (2016) reported that the kappa index κ fitted at ~0.1–1.5 keV is strongly correlated with the kinetic temperature T^*, while κ is negatively correlated with the sunspot number (SSN), for both the strahl and halo at quiet times. Wang et al. (2012, 2015) found that the quiet-time superhalo electrons observed at ~2–200 keV have a power-law energy spectrum, $J \propto E^{-\beta}$, with an average β of ~2.4 and show no solar-cycle variation.

Recently, Zhao et al. (2017) proposed a new classification scheme to categorize the types of coronal source region (CSR) of solar wind, based on the EUV brightness of the coronal structures associated with the back-mapped solar wind footpoints via the Potential Field Source Surface (PFSS) model (e.g., Wang & Sheeley 1992). Here we statistically investigate the energy spectrum of solar wind strahl, halo and superhalo electrons observed at 1 au by Wind/3DP at quiet times from 1998 to 2014, according to the types of their PFSS-mapped CSRs, to further investigate the origin/formation of solar wind suprathermal electrons.

Original content from this work may be used under the terms of the Creative Commons Attribution 4.0 licence. Any further distribution of this work must maintain attribution to the author(s) and the title of the work, journal citation and DOI.

2. Data and Methods

In the Wind/3DP instrument at 1 au, electron electrostatic analyzers (EESA–L and EESA–H) and silicon semiconductor telescopes (SST), respectively, provide the three-dimensional distribution measurements of electrons at energies of ~3 eV–30 keV and ~25–400 keV. The three-dimensional electron data are binned into eight pitch-angle (PA) bins with a resolution of 22°.5 (Wang 2009), according to the magnetic field direction measured by the Magnetic Field Investigation instrument (Lepping et al. 1995).

In this Letter, we utilize the ~0.1–1.5 keV (~20–200 keV) electron data from EESA (SST) at quiet times to study the strahl/halo (superhalo) electrons in the solar wind, while the measurements of ~2–20 keV are often dominated by the instrumental background in EESA–H at quiet times. As defined by Wang et al. (2015), we identify the ⩾12 hr quiet-time periods when the ~20–200 keV electron measurements show no significant temporal variation. Figures 1(b)–(e) shows a quiet-time period of suprathermal electrons observed by Wind/3DP on 2014 July 12. At energies below ~2 keV, the strahl is streaming antisunward along the interplanetary magnetic field (IMF) at PA $< 50°$, while the halo appears dominant at other PAs. At energies above 20 keV, the observed superhalo is nearly isotropic in angular distribution.

2.1. Sample Selection

For each quiet-time period, we select a 12 hr sample per day (see Figure 1, for example) and calculate the average suprathermal electron flux during such a sample. At ~0.1–1.5 keV (Tao et al. 2016), we average the electron data in the two PA bins perpendicular to the IMF to obtain the mean flux of the halo, $J_{\rm halo}$, assuming that the halo is nearly isotropic in angular distribution (e.g., Feldman et al. 1975); we subtract $J_{\rm halo}$ from the average flux in the two PA bins that are close to the field-aligned antisunward direction to obtain the mean flux of the strahl, $J_{\rm strahl}$. At ~20–200 keV, we average the omnidirectional data to get the mean flux of the superhalo, $J_{\rm sup}$, after removing the estimated instrumental background $J_{\rm bcg}$ due to cosmic rays.

After searching through the Wind/3DP electron data in the solar wind from 1998 to 2014, we obtain 255 (208) quiet-time samples of strahl/halo (superhalo) electrons that satisfy the constraint of $J_{\rm strahl}/J_{\rm halo}$ ratio >0.5 at all energies of ~0.1–1.5 keV (the constraint of $J_{\rm sup}/J_{\rm bcg}$ ratio >10 at at least four energies within ~20–200 keV; Wang et al. 2015; Tao et al. 2016), and have a PFSS-mapped CSR that can be unambiguously identified by the classification scheme of Zhao et al. (2017).

2.2. CSRs of Suprathermal Electrons

Solar wind suprathermal electrons travel generally in the same magnetic flux tube, but much faster compared to the solar wind plasma. Assuming that the CSR of suprathermal electrons does not significantly evolve on a scale of $\lesssim$5 days (Wang et al. 2012), we can take the PFSS-mapped CSR of in situ solar wind plasma as the CSR of in situ suprathermal electrons. Following the classification scheme of the solar wind CSR developed by Zhao et al. (2017), here we use the solar wind plasma measured by ACE/SWEPAM (McComas et al. 1998) to identify the CSR of suprathermal electrons measured by Wind/3DP, given the close locations of ACE and Wind. For each CSR, we also analyze the O^{7+}/O^{6+} ratio measured by ACE/SWICS (Gloeckler et al. 1998) prior to 2011 August 23 (when such measurements were unaffected by the space-weather-induced hardware anomaly; Gilbert et al. 2015).

First, we map the 2 hr average solar wind plasma back to their magnetic footpoints on the solar surface via the classic PFSS method (e.g., Wang & Sheeley 1992), and identify the coronal structures associated with such footpoints in the synoptic images of the Solar and Heliospheric Observatory/EIT 195 Å (from 1998 to 2006; Delaboudinière et al. 1995) or images of STEREO/SECCHI 195 Å (from 2007 to 2014; Howard & Tappin 2008) as the CSRs of 2 hr average solar wind. Second, we classify these CSRs into four types based on the brightness of image pixels and the perpendicular distance to the heliospheric current sheet (Figure 1(f)): helmet-streamer associated region (HS), active region including its boundary (AR), quiet Sun (QS), and coronal hole including its boundary (CH), in descending order of median value of O^{7+}/O^{6+} ratios (Zhao et al. 2017). A 12 hr sample of suprathermal electrons would correspond to six CSRs of 2 hr solar wind (Figure 1(f)). Finally, only if a CSR type occurs more than four out of the six times during the 12 hr sample window, we define such a type as the CSR type for this sample of suprathermal electrons.

2.3. Solar Wind Suprathermal Electrons

For the selected samples of strahl/halo, we fit both $J_{\rm strahl}$ and $J_{\rm halo}$ at ~0.1–1.5 keV to a kappa distribution function (Figure 1(a)) described as (e.g., Pierrard & Lazar 2010)

$$J(E) = \frac{En_0}{\pi m_e^{1/2}(2\kappa - 3)k_{\rm B}T^*)^{3/2}} \frac{\Gamma(\kappa+1)}{\Gamma(\kappa-\frac{1}{2})\Gamma(3/2)} \times \left(1 + \frac{2E}{(2\kappa-3)k_{\rm B}T^*}\right)^{-(\kappa+1)}, \quad (1)$$

where κ is the kappa index, n_0 is the number density of the entire function, and T^* is the kinetic temperature defined in the Tsallis statistical mechanics (Livadiotis 2015). Furthermore, we numerically integrate the kappa fit to $J_{\rm strahl}$ ($J_{\rm halo}$) over the energy range of ~0.1–1.5 keV to estimate the number density of strahl (halo):

$$n_{\rm strahl} = 2\pi(1 - \cos\frac{\pi}{4})\int_{0.1\ \rm keV}^{1.5\ \rm keV} \frac{J_{\rm strahl}(E)}{v}\, dE$$
$$n_{\rm halo} = 4\pi\int_{0.1\ \rm keV}^{1.5\ \rm keV} \frac{J_{\rm halo}(E)}{v}\, dE. \quad (2)$$

For the selected superhalo samples, we fit $J_{\rm sup}$ at ~20–200 keV to a power-law function (Figure 1(a)), $J \propto E^{-\beta}$, with a power-law index β. We integrate the fitted power-law function over the energy range of ~20–200 keV to estimate the superhalo number density:

$$n_{\rm sup} = 4\pi\int_{20\ \rm keV}^{200\ \rm keV} \frac{J_{\rm sup}(E)}{v}\, dE. \quad (3)$$

In order to compare among the suprathermal electrons of different solar origins, we divide the quiet-time strahl, halo, and superhalo samples, respectively, into four groups according to the type of their associated CSRs: i.e., HS-strahl, AR-halo, QS-superhalo, etc.

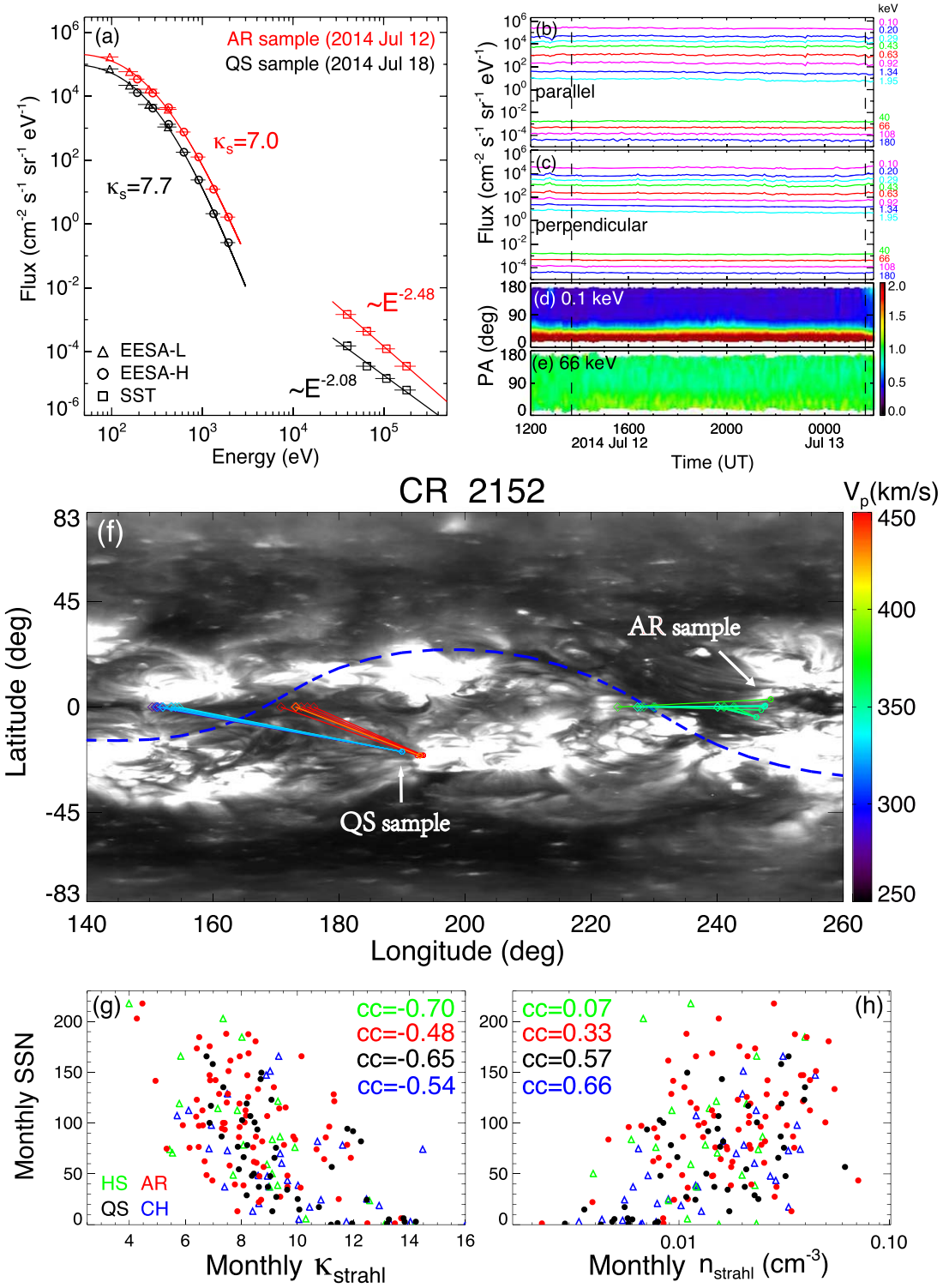

Figure 1. (a) Average energy spectra of the ∼0.1–1.5 keV strahl and ∼20–200 keV superhalo for the 2014 July 12 (red) and July 18 (black) samples. (b)–(c) 5 minute average fluxes vs. time of ∼0.1–200 keV electrons traveling parallel/perpendicular to the IMF measured by Wind/3DP on 2014 July 12–13. (d)–(e) 0.1 and 66 keV electron PA distributions normalized by the PA-averaged flux for each time bin. In (b)–(e), the dashed vertical lines indicate the 12 hr window of a selected sample centered at 1940 UT (the 2014 July 12 sample). (f) PFSS-mapping results of five quiet-time samples onto the STEREO/SECCHI synoptic map during Carrington Rotation 2152 (2014 June 28–July 25). The straight lines connect the 2 hr average locations of the ACE spacecraft traced along the Parker's spiral back onto the 2.5 R_s source surface (diamonds) and their PFSS-mapped footpoints on the solar surface (dots), color-coded by the solar wind speed measured by ACE/SWEPAM. The blue dashed line represents the magnetic neutral line at the source surface. The arrows indicate the CSRs of the two samples shown in panel (a). (g)–(h) Scatter plots of the monthly SSN vs. the κ_{strahl} and n_{strahl} of the monthly averaged quiet-time strahl. In (g)–(h), green, red, black, and blue colors represent the HS-strahl, AR-strahl, QS-strahl, and CR-strahl, respectively.

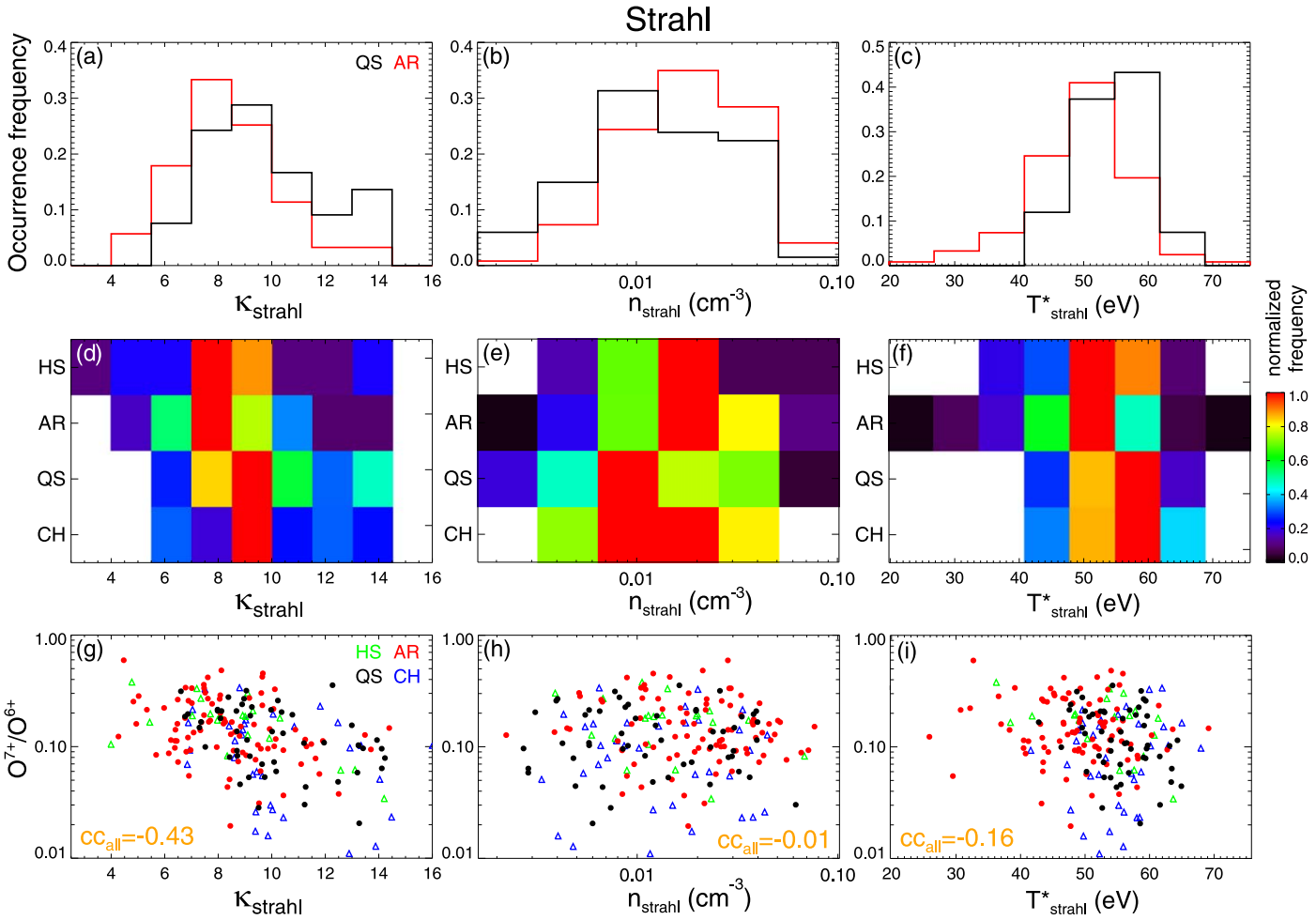

Figure 2. Statistical results of quiet-time strahl samples associated with each CSR type. (a)–(c) Histograms of the occurrence frequency of κ_{strahl}, n_{strahl}, and T^*_{strahl} for the QS-strahl (black) and AR-strahl (red). (d)–(f) Spectrograms of the distribution of κ_{strahl}, n_{strahl}, and T^*_{strahl}, normalized by the maximum occurrence frequency, for each CSR type (shown as a row). (g)–(i) Scatter plots of the O^{7+}/O^{6+} ratio vs. κ_{strahl}, n_{strahl}, and T^*_{strahl}. In (g)–(i), green, red, black, and blue colors represent the HS-strahl, AR-strahl, QS-strahl, and CR-strahl, respectively. The shown correlation coefficients are calculated for all the samples.

3. Statistical Results

3.1. Strahl

Figure 2 shows that in the κ_{strahl} index, kinetic temperature T^*_{strahl} and number density n_{strahl}, the AR-strahl and QS-strahl show different distribution histograms, as supported by the two-dimensional Kolmogorov–Smirnov (KS) test (Press et al. 2007); the HS-strahl distribution appears similar to the AR-strahl distribution, and the CH-strahl distribution seems like the QS-strahl distribution. In a statistical sense, the AR-strahl has a smaller κ_{strahl} with the most frequent value of 7–8.5, a smaller T^*_{strahl} with the most frequent value of 48–55 eV, and a larger n_{strahl} with the most frequent value of 0.013–0.026 cm^{-3}, while the QS-strahl has a larger κ_{strahl} with the most frequent value of 8.5–10, a larger T^*_{strahl} with the most frequent value of 55–62 eV, and a smaller n_{strahl} with the most frequent value of 0.006–0.013 cm^{-3}. These indicate that the AR-strahl could result from a more efficient acceleration. Note that such n_{strahl} (T^*_{strahl}) is smaller (larger) than that reported by Wilson et al. (2019a, 2019b, 2020) in the upstream region of interplanetary shocks, probably because the present study utilizes the electron measurements only at ~0.1–1.5 keV.

For each CSR type, κ_{strahl} shows a weak anticorrelation with the O^{7+}/O^{6+} ratio that is indicative of the coronal electron temperature (Zurbuchen 2007), despite that the statistical correlations may be somewhat misleading (e.g., Simpson 1951). HS-strahl, AR-strahl, QS-strahl, and CH-strahl have a mean value of O^{7+}/O^{6+} in descending order (not shown), consistent with the descending median value of O^{7+}/O^{6+} of solar wind originating from HS, AR, QS, and CH (Zhao et al. 2017). On the other hand, both n_{strahl} and T^*_{strahl} exhibit no obvious correlation with the O^{7+}/O^{6+} ratio.

For each CSR type, κ_{strahl} has a strong positive correlation with T^*_{strahl}, while neither κ_{strahl} nor T^*_{strahl} is associated with n_{strahl} (not shown). κ, T^*_{strahl}, and n_{strahl} all exhibit no obvious association with the solar wind speed V_{sw} at 250–750 km s^{-1} (left column of Figure 3). κ_{strahl} (and T^*_{strahl}) is clearly associated with the monthly SSN (Figure 1(g)). These are consistent with the previous study of quiet-time observations by Tao et al. (2016). n_{strahl} has an obvious association with the monthly SSN for the QS-strahl and CH-strahl (Figure 1(h)), but it shows no correlation (a weak correlation) with the monthly SSN for the HS-strahl (AR-strahl).

3.2. Halo

In κ_{halo} and T^*_{halo} (Figure 3), the AR-halo and QS-halo show different distributions, as supported by the two-dimensional KS test; the HS-halo appears indistinguishable from the AR-halo,

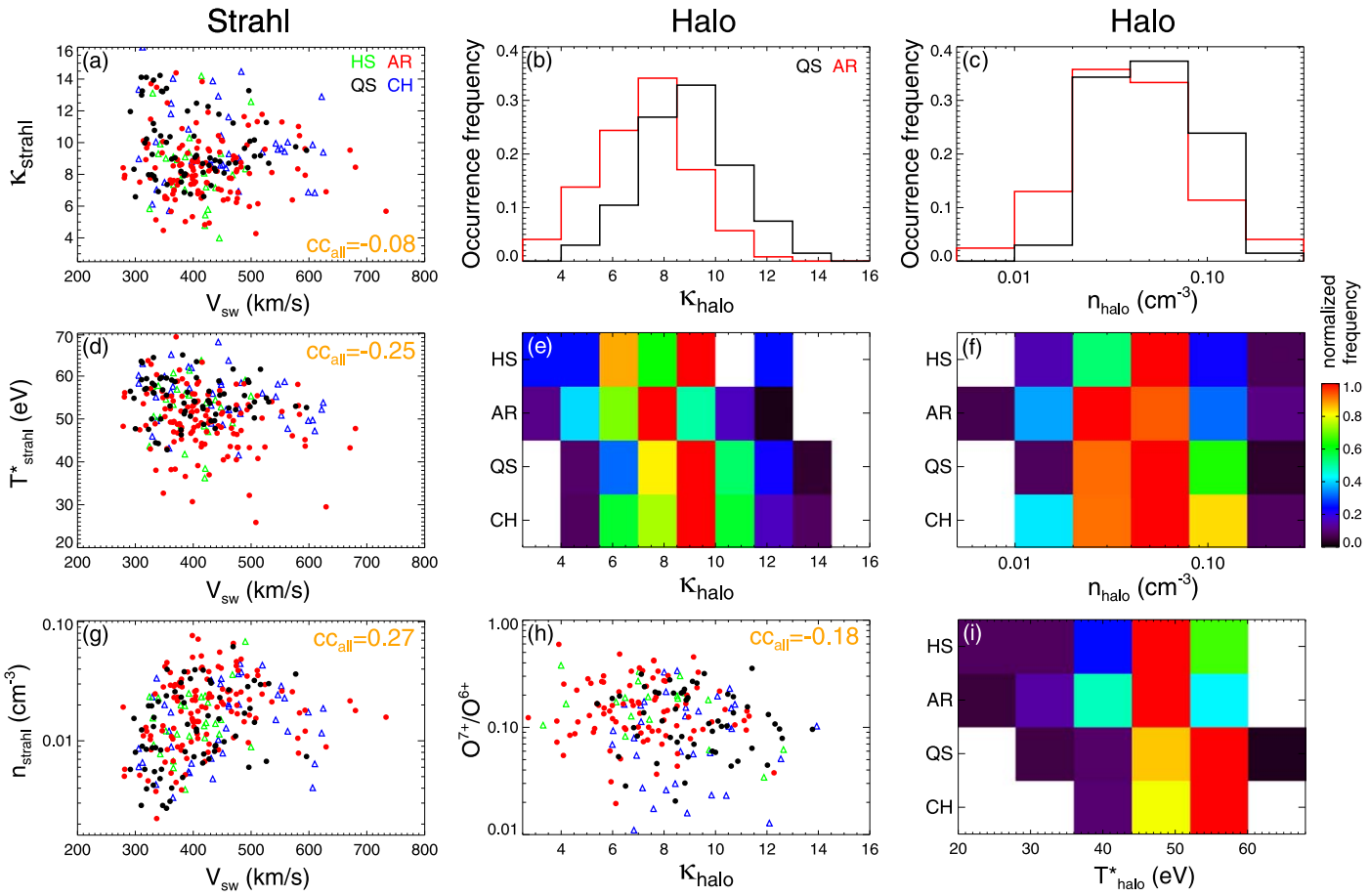

Figure 3. Left: scatter plots of $\kappa_{\rm strahl}$ (a), $n_{\rm strahl}$ (d), and $T^*_{\rm strahl}$ (g) vs. $V_{\rm sw}$. Middle and right: statistical results of $\kappa_{\rm halo}$, $n_{\rm halo}$, and $T^*_{\rm halo}$ of quiet-time halo samples associated with each CSR type, in the same format as Figure 2.

and the CH-halo seems similar to the QS-halo. In a statistical sense, the AR-halo has a smaller $\kappa_{\rm halo}$ ($T^*_{\rm halo}$) with the most frequent value of 7–8.5 (44–52 eV), while the QS-halo has a larger $\kappa_{\rm halo}$ ($T^*_{\rm halo}$) with the most frequent value of 8.5–10 (52–60 eV). These results are similar to those of quiet-time strahl. However, all four types of quiet-time halo behave similarly in $n_{\rm halo}$ with the most frequent value of 0.02–0.08 $\rm cm^{-3}$ (right column of Figure 3), different from the quite-time strahl.

For each CSR type, $\kappa_{\rm halo}$, $T^*_{\rm halo}$, and $n_{\rm halo}$ all show no clear association with the O^{7+}/O^{6+} ratio that is indicative of the coronal temperature (Figure 3) and $V_{\rm sw}$ (not shown). $\kappa_{\rm halo}$ and $T^*_{\rm halo}$ have a clear negative correlation with the monthly SSN, while $n_{\rm halo}$ shows no solar-cycle variation (not shown).

3.3. Superhalo

In the power-law index β (left panel of Figure 4), the AR-superhalo and QS-superhalo show different distributions, as supported by the two-dimensional KS test; both the HS-superhalo and CH-superhalo appear similar to either the AR-superhalo or the QS-superhalo. In a statistical sense, the AR-superhalo has a larger β with the most frequent value of 2.2–2.4, while the QS-superhalo has a smaller β with the most frequent value of 1.8–2.0. This indicates that the QS-superhalo could undergo a more efficient acceleration than the AR-superhalo, opposite to the efficiency of strahl acceleration. On the other hand, all four types of quiet-time superhalo behave similarly in $n_{\rm sup}$ (as supported by the KS test), with the most frequent value of 3×10^{-8}–3×10^{-7} $\rm cm^{-3}$ (right of Figure 4). For each CSR type, both β and $n_{\rm sup}$ show no association with the O^{7+}/O^{6+} ratio, $V_{\rm sw}$ and SSN.

3.4. Comparison among the Strahl, Halo, and Superhalo

For each CSR type, the strahl and halo are strongly correlated in κ, n (top panels of Figure 5), and T^* (not shown). $\kappa_{\rm halo}$ is similar to (smaller than) $\kappa_{\rm strahl}$ in ~70% (~30%) of quiet-time samples. In addition, the ratio of $n_{\rm halo}$ to $n_{\rm strahl}$ is less than 1 in ~7% of quiet-time samples, between 1 and 5 in ~69%, and larger than 5 in the other ~24%. Such large ratios of $n_{\rm halo}$ to $n_{\rm strahl}$, consistent with previous studies (Maksimovic et al. 2005; Tao et al. 2016), are likely due to the fact that the strahl is streaming only once from the Sun, but the halo could be a mixture of the scattered strahl in the IPM (e.g., Halekas et al. 2020). For each CSR type, the superhalo shows no association with both the strahl and halo in the spectral index and number density. These suggest that the superhalo likely has a origin different from that of the strahl and halo.

4. Summary and Discussion

We statistically examine the energy spectrum of solar wind strahl/halo electrons at ~0.1–1.5 keV and superhalo electrons at ~20–200 keV measured by Wind/3DP during quiet times from 1998 to 2014, according to the types of their PFSS-mapped CSRs (HS, AR, QS, and CH). We find that for the strahl, the AR-strahl (QS-strahl) has a smaller (larger) $\kappa_{\rm strahl}$ with the

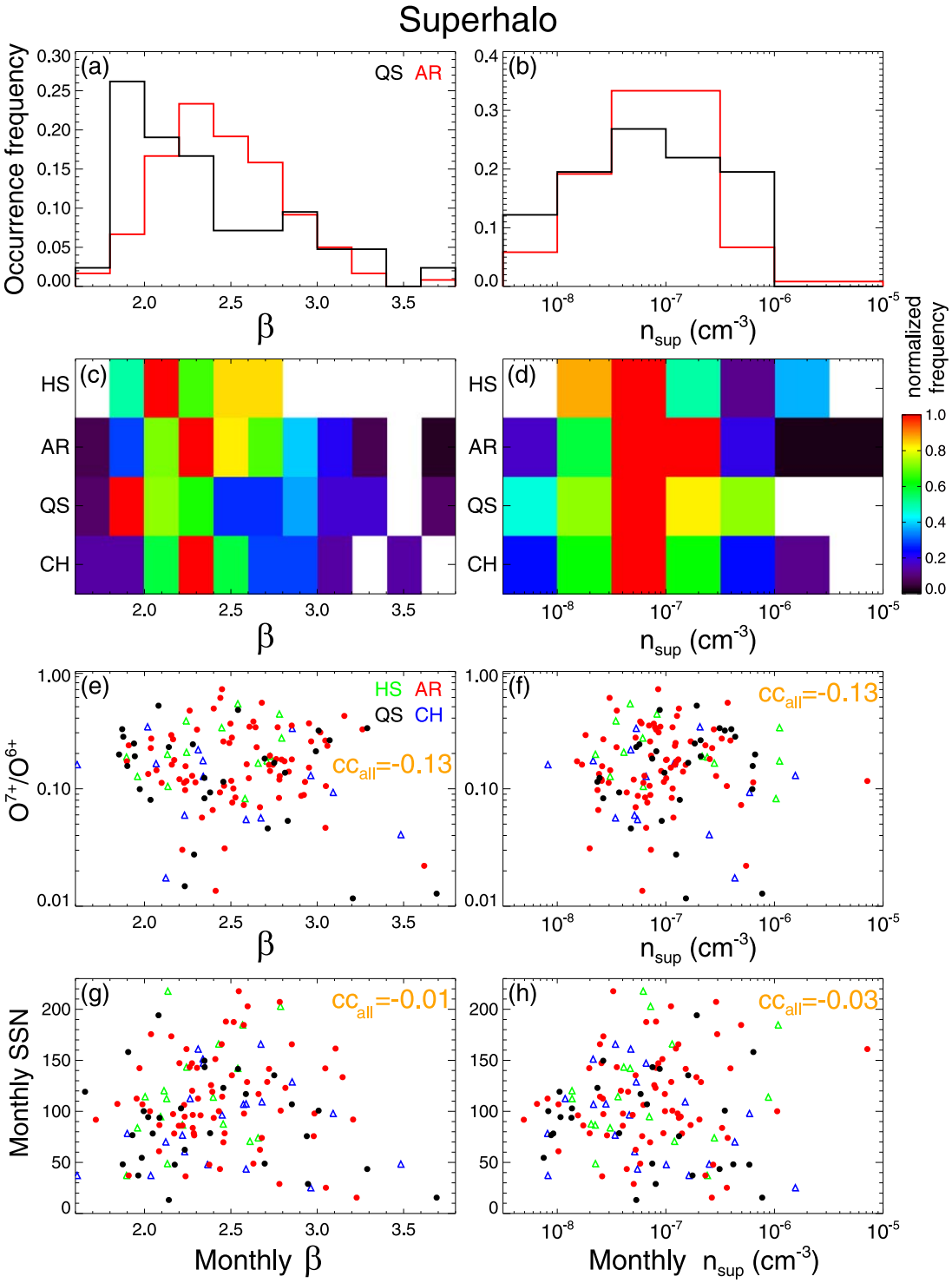

Figure 4. Statistical results of β and n_{sup} of quiet-time superhalo samples associated with each CSR type, in a similar format to Figure 2 and the bottom panels of Figure 1.

most frequent value of 7–8.5 (8.5–10), a smaller (larger) T^*_{strahl} with the most frequent value of 48–55 eV (55–62 eV), and a larger (smaller) n_{strahl} with the most frequent value of 0.013–0.026 cm^{-3} (0.006–0.013 cm^{-3}); the HS-strahl appears similar to the AR-strahl, and the CH-strahl seems like the QS-strahl. For the halo, κ_{halo} behaves similarly to κ_{strahl}, but n_{halo} appears similar among the four CSR types. For the superhalo, the AR-superhalo (QS-superhalo) has a larger (smaller) β with the most frequent value of 2.2–2.4 (1.8–2.0); n_{sup} appears similar with the most frequent value of 3×10^{-8}–3×10^{-7} cm^{-3} among the four CSR types. These results can help us better understand the origin and formation of solar wind strahl, halo, and superhalo electrons.

For the quiet-time strahl samples, the hot HS and AR have a smaller κ_{strahl} and a larger n_{strahl}, compared to the cold QS and CH. κ_{strahl} is also negatively associated with the O^{7+}/O^{6+} ratio (that is indicative of the coronal electron temperature). These observations support the idea that the strahl originates from

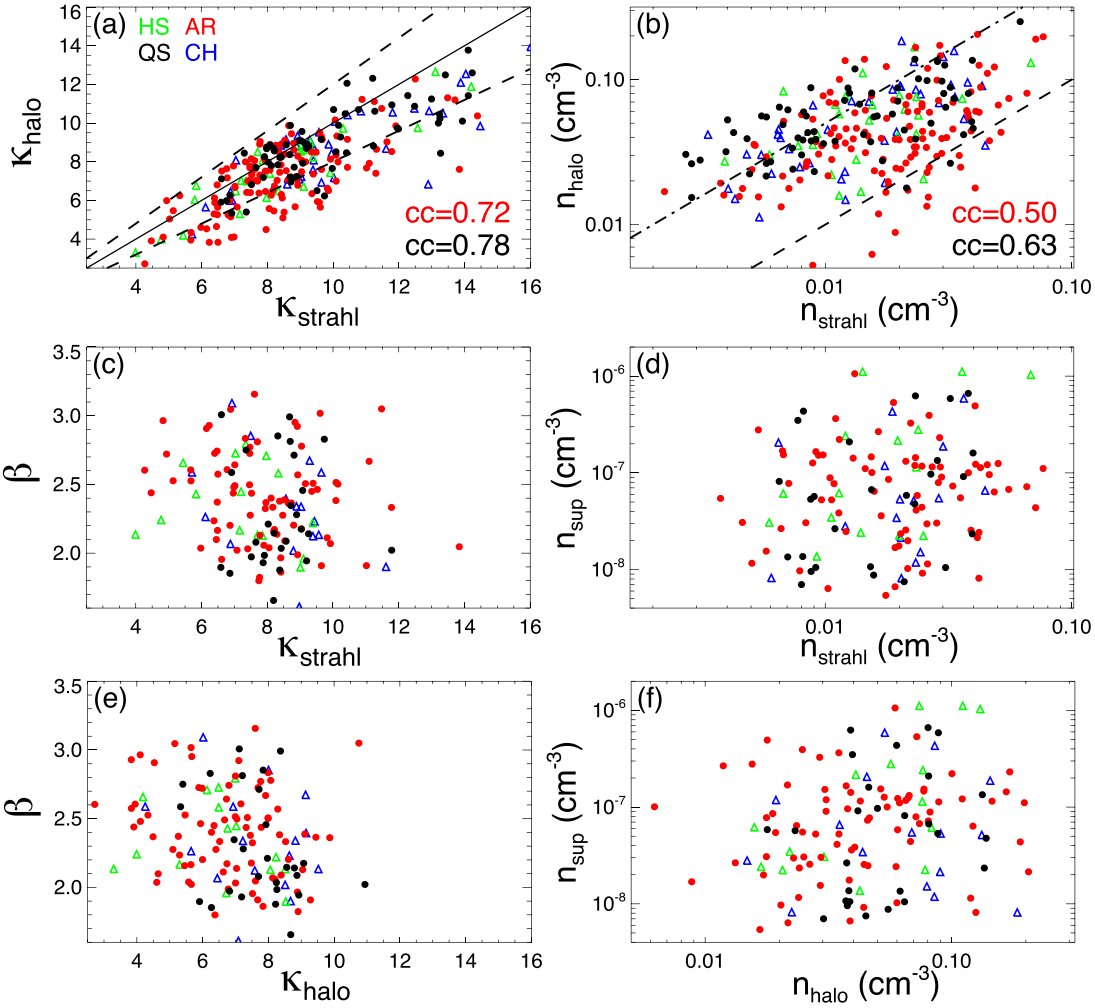

Figure 5. Scatter plots of $\kappa_{\rm strahl}$ vs. $\kappa_{\rm halo}$ (a), $n_{\rm strahl}$ vs. $n_{\rm halo}$ (b), the superhalo β vs. $\kappa_{\rm strahl}$ (c), $n_{\rm sup}$ vs. $n_{\rm strahl}$ (d), β vs. $\kappa_{\rm halo}$ (e), and $n_{\rm sup}$ vs. $n_{\rm halo}$ (f). In (a), the solid diagonal line represents the 1:1 ratio of $\kappa_{\rm halo}$ to $\kappa_{\rm strahl}$, and the two dashed lines indicate its $\pm 20\%$ variation range. In (b), the dashed (dashed–dotted) line represents a 1:1 (5:1) ratio of $n_{\rm halo}$ to $n_{\rm strahl}$.

escaping thermal electrons from the corona (e.g., Feldman et al. 1975; Pilipp et al. 1987; Maksimovic et al. 2005; Tao et al. 2016), since a hotter temperature likely leads to a more efficient escaping of thermal electrons. For each CSR type, both $\kappa_{\rm strahl}$ and $n_{\rm strahl}$ show a solar-cycle variation, probably due to the solar-cycle variation of the coronal temperatures (e.g., Altrock 2004; Schwadron et al. 2011).

For each CSR type, $\kappa_{\rm strahl}$ is also strongly correlated with $T^*_{\rm strahl}$, consistent with the previous study by Tao et al. (2016), but $T^*_{\rm strahl}$ has no clear association with the coronal electron temperature (indicated by the O^{7+}/O^{6+} ratio). This suggests that the strahl formation likely involves some acceleration process that can produce a kappa function of electron spectrum with a positive correlation between $\kappa_{\rm strahl}$ and $T^*_{\rm strahl}$ and become more efficient in the hot CSRs (e.g., AR) than the cold CSRs (e.g., QS).

For the quiet-time halo, the hot HS and AR (the cold QS and CH) correspond to a smaller (larger) $\kappa_{\rm halo}$, and $\kappa_{\rm halo}$ shows a solar-cycle variation, similar to the quiet-time strahl. Unlike the quite-time strahl, however, all four CSR types seem to have a similar $n_{\rm halo}$ with the most frequent value of 0.02–0.08 $\rm cm^{-3}$, $\kappa_{\rm halo}$ has no clear association with the O^{7+}/O^{6+} ratio, and $n_{\rm halo}$ shows no solar-cycle variation. In addition, for each CSR type, the halo is strongly correlated with the strahl in κ, T^*, and n. These support the idea that the halo is likely formed by scattering of the strahl in the IPM (e.g., Pilipp et al. 1987; Maksimovic et al. 2005; Tang et al. 2020). Such interplanetary scattering processes would retain most of the CSR signatures in the spectral shape of strahl, but smear out the CSR signatures in number density.

The quiet-time superhalo is not correlated with either the strahl or halo. The QS-superhalo also shows a smaller power-law index β than the AR-superhalo, while β shows no association with the coronal electron temperature (indicated by the O^{7+}/O^{6+} ratio). These imply that the superhalo can originate from some acceleration process at the Sun, rather than from some acceleration process acting on the strahl and halo in the IPM. Such acceleration may occur at lower altitudes, rather than in the corona. As proposed by Wang et al. (2012, 2015), the superhalo can be accelerated by nonthermal processes in the solar wind source region, e.g., the magnetic reconnection (Yang et al. 2015b), followed by an isotropization due to strong scattering/reflection in the IPM, e.g., by waves and/or turbulence (Vocks et al. 2005; Fisk & Gloeckler 2006; Ragot 2006; Yoon et al. 2012). This formation may require a more efficient acceleration in the QS than in the AR, while the interplanetary scattering can mix out the CSR signatures in $n_{\rm sup}$

and produce a nearly isotropic angular distribution of superhalo (Yang et al. 2015a).

The research at Peking University is supported in part by NSFC under contracts 41861134033, 41774183, 41421003, 41574168, and 41874200. L.Z. is supported by NSF awards AGS-1621686 and NASA grants NNX16AT39G, 80NSSC18K0275, 80NSSC18K1553, and 80NSSC18K0645. G.L. is supported in part by NASA grants 80NSSC19K0075 and 80NSSC19K0079. R.W.S. thanks the German space agency DLR for support under grants 50 OT 1201, 50 OT 1501, and 50 OT 1701. S.B. is supported in part under NASA grant 80NSSC20K0057. L.W. and G.L. also acknowledge support from the ISSI-BJ and ISSI through the international teams 469 and 425.

ORCID iDs

Liu Yang https://orcid.org/0000-0002-6416-1538
Linghua Wang https://orcid.org/0000-0001-7309-4325
Liang Zhao https://orcid.org/0000-0002-5975-7476
Gang Li https://orcid.org/0000-0003-4695-8866
Robert F. Wimmer–Schweingruber https://orcid.org/0000-0002-7388-173X
Jiansen He https://orcid.org/0000-0001-8179-417X
Hui Tian https://orcid.org/0000-0002-1369-1758
Stuart D. Bale https://orcid.org/0000-0002-1989-3596

References

Altrock, R. C. 2004, SoPh, 224, 255
Chang, O., Gary, S. P., & Wang, J. 2013, JGRA, 118, 2824
Delaboudinière, J.-P., Artzner, G. E., Brunaud, J., et al. 1995, SoPh, 162, 291
Feldman, W. C., Asbridge, J. R., Bame, S. J., Montgomery, M. D., & Gary, S. P. 1975, JGR, 80, 4181
Fisk, L. A., & Gloeckler, G. 2006, ApJL, 640, L79
Fisk, L. A., Gloeckler, G., & Schwadron, N. A. 2010, ApJ, 720, 533
Gilbert, J. A., Shearer, P., & Zurbuchen, T. H. 2015, New and Updated Ion Composition Data Products from SWICS, ACE News, 177
Gloeckler, G., Cain, J., Ipavich, F. M., et al. 1998, SSRv, 86, 497
Halekas, J. S., Whittlesey, P., & Larson, D. E. 2020, ApJS, 246, 22
Howard, T. A., & Tappin, S. J. 2008, SoPh, 252, 373
Hughes, R. S., Gary, S. P., & Wang, J. 2014, GeoRL, 41, 8681
Kim, S., Yoon, P. H., Choe, G. S., & Wang, L. 2015, ApJ, 806, 32
Lepping, R. P., Acũna, M. H., Burlaga, L. F., et al. 1995, SSRv, 71, 207
Lin, R. P. 1998, SSRv, 86, 61
Lin, R. P., Anderson, K. A., Ashford, S., et al. 1995, SSRv, 71, 125
Livadiotis, G. 2015, JGRA, 120, 1607
Maksimovic, M., Pierrard, V., & Lemaire, J. F. 1997, A&A, 324, 725
Maksimovic, M., Zouganelis, I., Chaufray, J.-Y., et al. 2005, JGRA, 110, A09104
McComas, D. J., Bame, S. J., Barker, P., et al. 1998, SSRv, 86, 563
Montgomery, M. D., Bame, S. J., & Hundhausen, A. J. 1968, JGR, 73, 4999
Parker, E. N. 1988, ApJ, 330, 474
Pierrard, V., & Lazar, M. 2010, SoPh, 267, 153
Pierrard, V., Maksimovic, M., & Lemaire, J. 2001, Ap&SS, 277, 195
Pilipp, W. G., Miggenrieder, H., Montgomery, M. D., et al. 1987, JGR, 92, 1075
Press, W. H., Teukolsky, S. A., Vetterling, W. T., & Flannery, B. P. 2007, Numerical Recipes, The Art of Scientific Computing (3rd ed.; Cambridge: Cambridge Univ. Press)
Ragot, B. R. 2006, ApJ, 642, 1163
Saito, S., & Gary, S. P. 2012, PhPl, 19, 012312
Saito, S., Gary, S. P., Li, H., et al. 2008, PhPl, 15, 102305
Schwadron, N. A., Smith, C. W., Spence, H. E., et al. 2011, ApJ, 739, 9
Simpson, E. H. 1951, J. R. Stat. Soc. Ser. B, 13, 238
Štverák, Š., Maksimovic, M., Trávníček, P. M., et al. 2009, JGRA, 114, A05104
Tang, B., Zank, G. P., & Kolobov, V. I. 2020, ApJ, 892, 95
Tao, J., Wang, L., Zong, Q., et al. 2016, ApJ, 820, 22
Vocks, C., Salem, C., Lin, R. P., & Mann, G. 2005, ApJ, 627, 540
Wang, L. 2009, PhD thesis, Univ. of California
Wang, L., Lin, R. P., Salem, C., et al. 2012, ApJL, 753, L23
Wang, L., Yang, L., He, J., et al. 2015, ApJL, 803, L2
Wang, Y. M., & Sheeley, N. R. 1992, ApJ, 392, 310
Wilson, L. B., III, Chen, L.-J., Wang, S., et al. 2019a, ApJS, 243, 8
Wilson, L. B., III, Chen, L.-J., Wang, S., et al. 2019b, ApJS, 245, 24
Wilson, L. B., III, Chen, L.-J., Wang, S., et al. 2020, ApJ, 893, 22
Yang, L., Wang, L., Li, G., et al. 2015a, ApJL, 811, L8
Yang, L., Wang, L., Li, G., et al. 2018, ApJ, 853, 89
Yang, L., Wang, L., Li, G., et al. 2019, ApJ, 875, 104
Yang, L.-P., Wang, L.-H., He, J.-S., et al. 2015b, RAA, 15, 348
Yoon, P. H., Rhee, T., & Ryu, C.-M. 2006, JGRA, 111, A09106
Yoon, P. H., Ziebell, L. F., Gaelzer, R., Lin, R. P., & Wang, L. 2012, SSRv, 173, 459
Zank, G. P., Roux, J. A., Webb, G. M., et al. 2014, ApJ, 797, 28
Zhao, L., Landi, E., Lepri, S. T., et al. 2017, ApJ, 846, 135
Zurbuchen, T. H. 2007, ARA&A, 45, 297